Postprint of: Szkodo M., Gajowiec G., Studies of the mechanism of metal dusting of 10CrMo9-10 steel after 10 years of operation in the semi-regenerative catalytic reformer, Corrosion Science, Vol. 102 (2016), pp. 279-290, DOI: 10.1016/j.corsci.2015.10.016

Studies of the mechanism of metal dusting of 10CrMo9-10 steel after 10 years of operation in the semi-regenerative catalytic reformer

Marek Szkodo (corresponding author),
Gdansk University of Technology, Mechanical Engineering Faculty, 80-233 Gdansk, ul. G. Narutowicza 11/12, mszkodo@pg.gda.pl tel 666055620
Grzegorz Gajowiec,
Gdansk University of Technology, Mechanical Engineering Faculty, 80-233 Gdansk, ul. G. Narutowicza 11/12, speed1@wp.pl

ABSTRACT

The study showed that metal dusting mechanism of 10CrMo9-10 steel operated in industrial environment differs from models developed in laboratories. Significant differences lie in the fact that the models developed in laboratories only assume the formation of metastable carbide M_3C, while studies have shown that the formation of M_3C carbides is preceded by formation of the $M_{23}C_6$ carbides, which nucleate at primary carbides/metal matrix interfaces. Their growth results in a large spheroidal precipitates, and it is accompanied by a decrease chromium and molybdenum in the matrix, whereby the content of these elements in emerging carbides is getting lower.

Keywords: A. low alloy steel; B. SEM; B. TEM; C. carburization

1. Introduction

Corrosion of metals and alloys in industrial environments with high carbon activity - the so-called metal dusting, is a phenomenon known for more than 60 years. This phenomenon occurs mainly in thermo-chemical factories, metallurgical, petrochemical and refining industries [1-7]. A common feature of these environments is, along with the high carbon activity, the temperature of the order of 450-800 °C [8]. The first data on damage related to metal dusting been published by Camp in 1945 [9]. Superheater feedstock unit was damaged in a refinery naphtha reforming installation. In 1950, Burns made a series of case studies of corrosion of metal alloys under different environments in refinery plants [10]. He showed that in the case processing of crude oil with low sulfur content of 0.2% weight, there may be a significant loss corrosive crude distillation unit devices operating at temperatures up to about 400 °C. This problem has not been elucidated, it is likely that the cause of rapid progress of metal loss was the corrosion due to high activity of carbon atoms.
In recent years, much attention was paid to the metal dusting phenomenon in petrochemical installations. It is a frequent problem in the preparation of synthesis gas by reforming, where natural gas is replaced by a mixture of CO, H_2, CO_2 and H_2O. The synthesis gas is then used to produce hydrogen, ammonia, methanol and liquid hydrocarbons. In order to increase the efficiency of production processes perform at lower share of water vapor and greater participation of carbon

monoxide. Such modification of the process creates a more aggressive environment, the lower oxygen partial pressure and the higher carbon activity, promoting the development of metal dusting process [11]. In the reforming of natural gas installations, among others, nickel alloys and iron alloys, with the content of alloying elements, chromium and nickel are used. For these alloys, corrosion is particularly dangerous because it is selective. Formed pits are penetrating throughout the wall element in a short time. Pitting may occur within a few days, leading to considerable damage. An example of such "instant" failure, which occurred after the three-week operation, was presented by Eberle and Wylie, who analyzed the damage to the components of the boiler made of 25Cr-20Ni (310) and 18Cr-8Ni (347) steels operating under the synthesis gas in the range 400-950 °C [12].

About the fact that metal dusting is still an unsolved problem evidenced by the many publications appearing every year [27-30]

In the literature, several physical models explaining the course of metal dusting of Fe-base alloys can be find. For example, according to Natesan and his team [24], metal dusting proceeds in several stages. First, carbon deposits on the iron surface and supersaturates the ferrite. In the next step, Fe_3C forms at the surface. Cementite formation is accompanied by an increase in volume which results in the generation of crystalline defects. Further, carbon diffuses through the Fe_3C. Numerous defects in the crystal lattice of cementite improve the diffusion of carbon. Carbon atoms accumulate at cementite defects causing the Fe_3C particles to separate into small particles and to move away from the metal. In this model, the driving force for metal dusting is the free energy difference between good and poor crystalline carbon. Their physical model helps explain of metal dusting without decomposition of Fe_3C.

Another physical model was presented by Grabke [17]. According to this mechanism, within the temperature range 400 - 650 °C, active carbon atoms are dissolved in ferrite causing its supersaturation. Next, cementite nucleation starts at the carbon supersaturated ferrite. Fe_3C increases mainly on the metal surface but also at the grain boundaries. Cementite layer formed a barrier to further penetration of carbon into the metal because of its low diffusion coefficient in cementite. Therefore, the carbon activity on the surface increases and the graphite takes nucleation locally on the surface. Consequently, the carbon activity reduced to $a_c = 1$ which causes instability of cementite. In the next stage cementite breaks down into graphite and iron. The carbon atoms, from the decay of Fe_3C, join the graphite planes and iron atoms diffuse out through the graphite, and when the concentration rich 3-4%, agglomerate to form fine particles of Fe having a diameter of about 20 nm. Carbon, formed in further from the gas atmosphere, penetrates into the fine particles of iron. The carbon diffuses through the Fe particles to places where easily graphite nucleates. In these places, graphite begins to increase often in the form of fibers. The rate of growth of the carbon fibers and thus coke formation rate depends on the velocity of the carbon atoms in the iron particles.

In turn, Young and his group proposed still another physical model of metal dusting of pure iron and low alloy steels . According to them [25], mass transfer process involved is diffusion of gas through porous coke, and permeation of carbon through the cementite phase of the scale. Diffusion process is driven by activity gradients produced by contact with the gas. Carbon permeation supports transformation of iron to cementite at the alloy–scale interface, and inward scale growth. Carbon diffusion also leads to graphite formation near the surface. The resulting volume increase causes scale disintegration and the generation of dust.

Chun and Ramanarayanan [26] proposed their own metal dusting model of steel with a low chromium content. According to their model, metastable surface M_3C growth and its subsequent decomposition upon carbon deposition is the main corrosion mechanism. If the nature of the carbon deposit on the surface of M_3C is mostly graphitic, the graphite planes are oriented more or less perpendicular to the dissociating M_3C. Then iron atoms arising from M_3C dissociation intercalate into the graphite and diffuse outward to the carbon-supersaturated environment where they coalesce and catalyze filamentous-carbon formation. In the case when carbon deposit on the surface of M_3C is mostly amorphous, stress-induced fracturing of M_3C could occur in some regions since amorphous carbon does not provide a pathway for iron atoms from dissociated M_3C to escape. During the formation and growth of M_3C, stresses accumulate and lead the breakup of M_3C above a critical stress level. Once initial fracture of M_3C has occurred, corrosion preferentially continues in the same region.

Models available in the literature [13-18, 24-26] describing the mechanisms of metal dusting for low- and high-alloyed steels are based on laboratory tests, which do not reflect the operating parameters of these materials in industrial plants. Most of these studies, in order to quickly corrode, carried out in the atmospheres of carbon activity much higher compared to the atmosphere found in industrial installations, and durations were much shorter than the typical operating time of heat resistant steel in these plants. Long-term operation at high temperatures causes changes in the microstructure of these steels, including precipitation of carbides and intermetallic phases, carbide changes and changes in the distribution of alloying elements between matrix and precipitates (depletion of alloying elements in the matrix) which may affect the corrosion mechanism. Meanwhile adopted durations of experiments conducted in laboratory conditions were too short to these phenomena occurred, making it impossible to analyze their impact on the mechanism of metal dusting. Thus, the models describing the mechanisms of metal dusting corrosion, developed on the basis of laboratory tests do not fully describe the degradation mechanisms operating steel in industrial installations. These mechanisms can be determined based on the study of materials operating under industrial conditions, while conducting laboratory tests in conditions reflecting the operating parameters of these materials in industrial plants require time to the order of tens of thousands hours.

The analysis of the mechanism of metal dusting in an industrial environment is difficult due to the lack of to-date traceability changes in the structure of the material. Another problem is the determination of carbon activity. Calculation of the carbon activity is simple when, in laboratory conditions, exogenous gas is used with a specific content of components such as CO, CH_4, CO_2, H_2O. Then the most important reactions occurring during the process are following:

$2CO \rightarrow C + CO_2$,

$CH_4 \rightarrow C + 2H_2$,

$CO + H_2 \leftrightarrow C + H_2O$,

If the hydrocarbon concentration is high, to calculate the carbon activity can be used formula:

$$a_c = e^{-\Delta G/RT}\left(\frac{P_{CH_4}}{P_{H_2}^2}\right)$$

In the case of semi-regenerative reforming unit, feed is rich in dozens of hydrocarbons, and most of them can be reacted to activated carbon by contact with the surface of the steel. Depending on the hydrocarbon, reactions may occur such as:

$C_2H_2 \rightarrow 2C + H_2$,

$C_3H_8 \rightarrow C + 2CH_4$,

$C_3H_8 \rightarrow C_2H_4 + CH_4 \rightarrow C + 2CH_4$,

$C_3H_8 \rightarrow C_2H_2 + CH_4 + H_2 \rightarrow C + 2CH_4$,

$C_2H_4 \rightarrow C + CH_4$,

In addition, each of these reactions has its free energy and the kinetics of the reaction. The resulting products of these reactions are next carbon atoms, shorter hydrocarbons which can still be subject to further reactions. For this reason, it is impossible to determine the carbon activity in the gas atmosphere.

Metal dusting corrosion was identified in the furnace installation of semi-regenerative catalytic unit in a petroleum refinery in Gdansk (Grupa Lotos S.A.). After 10 years of operation of the furnaces on the inner surface of the pipe made of 10CrMo9-10 (P22 according to ASTM) steel, containing 2.25% Cr and 1% Mo, a thin layer of coke formed, containing graphite, iron and alloy carbides. The analysis of corrosion mechanism pointed to the metal dusting. Therefore, the carbon activity of the gas atmosphere had to be greater than unity. The corrosion was evenly in nature, and the pipe wall thickness was remaining in the range of dimensional tolerance of products. The corrosion rate was not catastrophic nature, which is usually in environments involving hydrogen, steam and carbon monoxide.

The purpose of this paper is to present a metal dusting mechanism for 10CrMo9-10 steel operated for 10 years in the semi-regenerative catalytic reformer.

2. Experimental procedure

The semi- regenerative catalytic reforming installation was operated in refinery in Gdansk (Poland). Typical diagram of such an installation is shown in Fig. 1a.

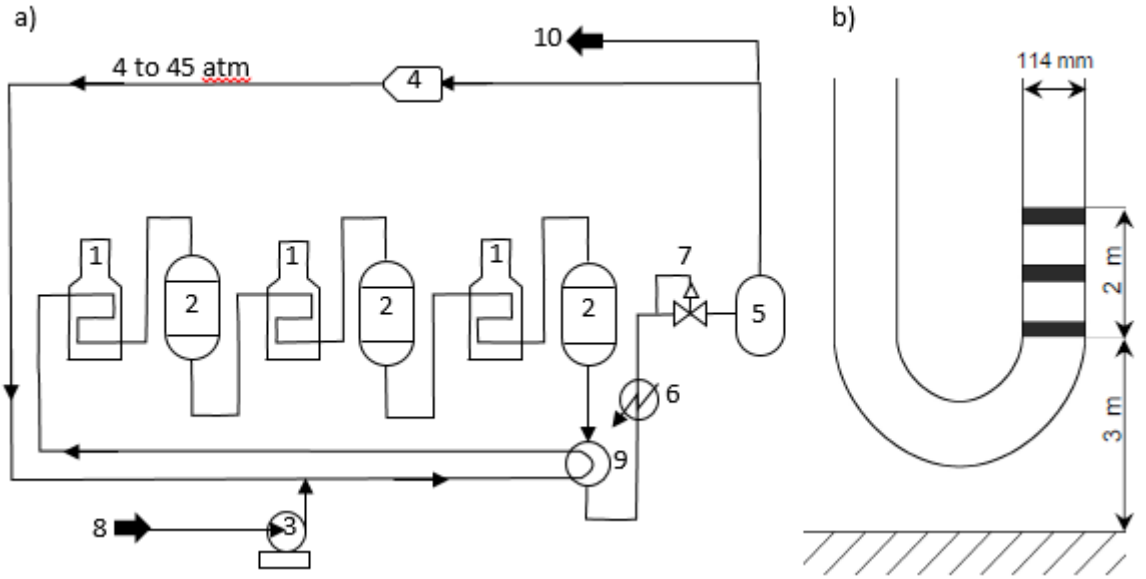

Fig. 1. Schematic diagram of a typical semi-regenerative catalytic unit in a petroleum refinery 1 – fired heater, 2 – fixed bed reactor, 3 – pump, 4 – compressor, 5 – gas separator, 6 – cooler, 7 – pressure controller, 8 – feed (hydrotreated naphtha and recycle hydrogen gas), 9 – preheater, 10 – net hydrogen – Fig. a), and the schema of the part of tailpipe furnace together with selected locations of samples for testing – Fig. b)

Four furnaces were in the reactor unit of the plant. The pipes of the fired heater were made of steel with a nominal content of chromium 2.25% and molybdenum 1% (P22 steel according to ASTM and 10CrMo9-10 according to PN-EN). After 10 years of operation from second furnace from zone in which there was the highest temperature (600 °C), fragment of approximately 2 meters of the exhaust pipe No 12 was cut out (Fig. 1b). Macroscopic studies have shown that the inner surface of the tube is coated with a thin and dark layer resembling a soot sediment (Fig. 2). Thickness measurements made on the piece of the pipe taken from the installation showed that the pipe wall thickness was close to the nominal value. Then from this pipe, sample for microscopy testing was taken. Metallographic examinations were performed on cross sections of the pipe, which the nominal diameter was 114.3 mm and wall thickness was equal to 6 mm. Table 1 shows characteristics of steel tested and the service conditions.

Fig. 2. View of cut portion of the tube furnace No 12

Metallographic examination of the samples taken of the material was performed using light microscopy, scanning electron microscopy and transmission electron microscopy respectively. In studies used a light microscope Leica Reichert MEF4M. Metallographic examination using the microscope was carried out in a bright field. The aim of the study was to determine the thickness of the carburized surface layer. In metallographic studies also was used Hitachi S4200 scanning electron microscope. The microstructure of the material pipe, at different distances from the inner surface of the tube, was determined by using of this microscope. This microscope was equipped with EDS X-ray spectrometer, by means of which the chemical composition was determined by collecting the signals

Table 1. Characteristics of steel tested and the service conditions

characteristics	description
Composition of steel (wt%)	C=0.11; Mn=0.58; Si=0.29, P=0.01; S=0.005; Cr=2.33; Mo=0.92
Feed	Hydrotreated naphtha and recycle hydrogen gas, sulphur content in the naphtha 0.25 ppm, H_2S content in the hydrogen <0.5 ppm, temperature in the last furnace 470 °C (start of service) to 520 °C (after 10 years of service)
Feed pressure	Hydrotreated naphtha ~0.70 MPag; hydrogen ~0.56 MPag
Metal skin temperature	~600 °C during the 10th year of service

both from designated areas and microstructural constituents. This approach allowed the determination of the average content of elements in the steel, and to identify the chemical composition of carbides located at different distances from the inner surface of the pipe. In metallographic studies also used transmission electron microscope JEM 100C, which was equipped with a scanning ASID 4-D attachment and X-ray spectrometer ISIS 300. A TEM studies were

conducted on the extraction replicas. For this purpose, the metallographic cross-section was made, which next was electrolytically etched. Then the carbon replicas were removed, on which were extracted carbides. Two areas were studied: near the inner surface of the pipe and from the center of the sample thickness. Microstructure observation was made at an accelerating voltage of 100 kV and analyzing of the chemical composition at 40 kV. Analyses were performed at different distances from the surface and from the carbides differ in shape and size. At the same time, there were made attempts to obtain the electron diffraction of the various types of carbides for their identification.

3. Results

Fig. 3a shows a cross-section of the tube wall. A carburized microstructure is visible below surface of the inner pipe. Its thickness is about 2 mm. Study of the microstructure using SEM revealed the morphology of the surface layer. The inner surface of the pipe is covered with a coke layer whose thickness is in the range from 5 to 15 µm. Directly beneath the inner tube, the thin, continuous layer of carbide having a thickness of about 1 - 2 µm (Fig. 3b) occurs. A characteristic feature of this layer is the presence of the developed coke/carbide layer interface (Fig. 3b). A plurality of cavity- shape like of the pits filled with corrosion products are present in this layer. This carbide layer structure proves that it disintegrates in the process of metal dusting.

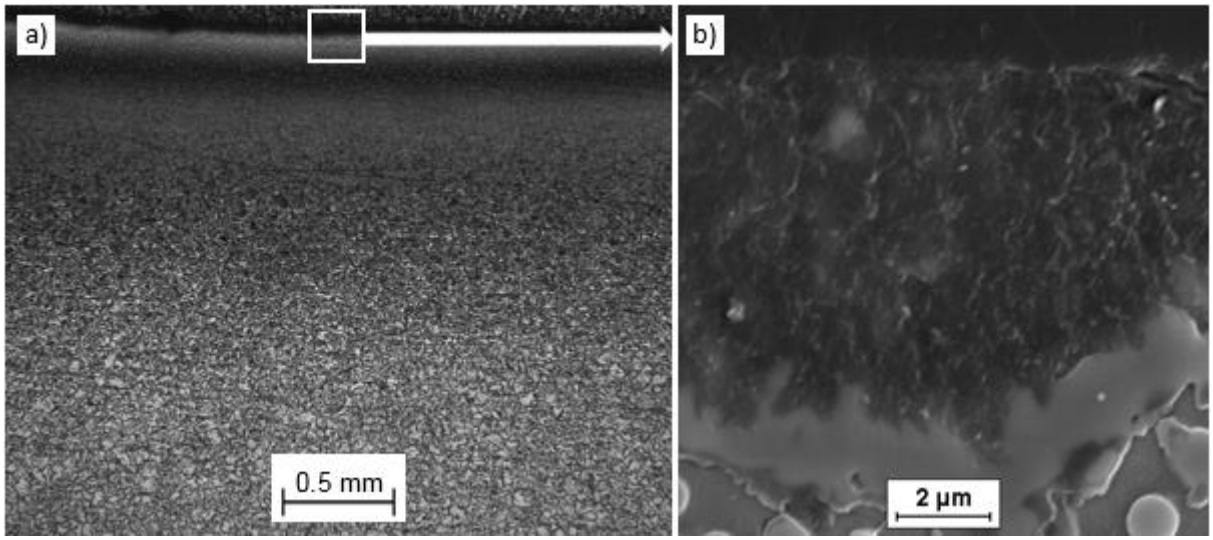

Fig. 3. The cross section of P22 steel pipe after 10 years of operation in the semi-regenerative catalytic reformer. The carburized layer for apprx 2 mm is visible (bright field, LM) – Fig. a), and image corrosion products and disintegration continuous layer of carbides (SEM) – Fig. b)

Fig. 4 shows the microstructures of the steel made at different distances from the inner surface of the pipe. Under inner surface of the pipe there are visible numerous, large spheroidal carbides evenly distributed in the ferritic matrix (Fig. 4a, b). With increasing distance from the inner surface of

the pipe, carbides contribution in the microstructure of the steel and their size are reduced. Also their structure changes - already at a depth of 150 µm lamellar carbides can be observed (Fig. 4b), which part increases with the distance from the inner surface.

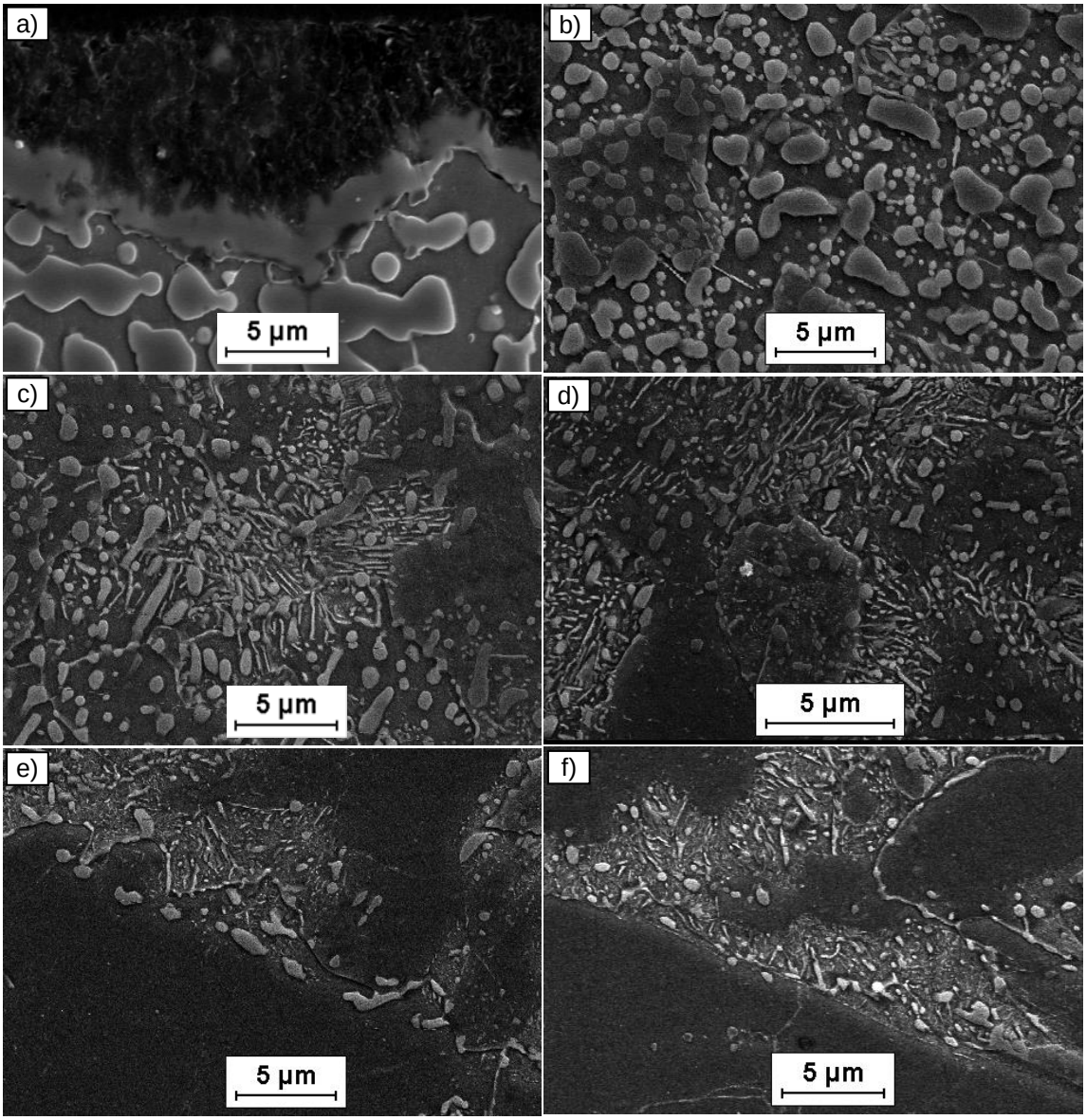

Fig. 4. Images obtained with the cross section of the tube. The inner surface of the pipe with the subsurface layer – Fig. a). Microstructure of the steel approximately 150 µm from the inner surface of the pipe – Fig. b), 500 µm from the surface – Fig. c), 750 µm from the surface – Fig. d), 1 mm from the surface – Fig. e), 3 mm from the surface – Fig. f)

Carbon content analysis using EDS techniques are subject to large uncertainties, therefore, in order to determine the approximate distribution of carbon in the carburized layer, tests of the distribution of alloying elements - Cr and Mo, were carried out. These elements have a greater affinity to carbon than the iron. Distribution of alloying elements between carbides and ferrite matrix is different,

therefore, in order to determine the average content of these elements in the steel at different distances from the inner surface of the tube, analyzes were performed in areas with dimensions of about 40 µm x 140 µm. The results of these analyzes are shown in Table 2 and in a Fig. 5.

Table. 2. The content of elements at different distances from the inner surface of the tube measured by EDS

the distance from the surface [µm]	element				
	Si	Cr	Mn	Fe	Mo
0	3.90	2.67	0.58	91.23	1.62
40	2.28	2.81	0.00	94.16	0.75
110	2.17	2.49	0.64	93.62	1.08
190	1.98	2.60	0.46	94.96	0.00
260	2.15	2.25	0.93	94.67	0.00
340	2.04	2.67	0.00	94.31	0.98
400	2.06	2.55	0.50	94.24	0.65
500	2.23	2.38	0.00	94.48	0.91
580	2.06	2.61	0.54	93.64	1.15
660	2.20	2.60	0.51	93.63	1.06
740	1.90	2.45	0.67	93.89	1.09
830	2.12	2.72	0.52	94.00	0.64
average	**2.26**	**2.57**	**0.45**	**93.90**	**0.83**

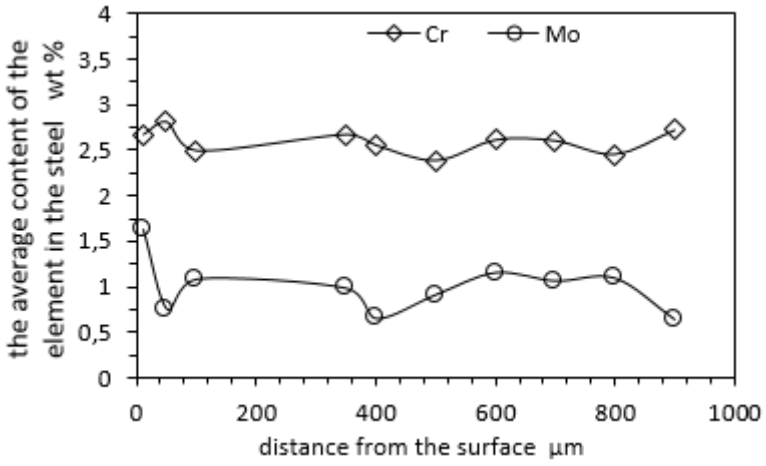

Fig. 5. Average content of the chromium and molybdenum in the steel as a function of distance from the inside surface (IS) of the tube measured by EDS

As is apparent from Fig. 5 the average content of the alloying elements Cr and Mo as a function of distance from the surface of the inner pipe is approximately constant. There is no the outward diffusion of elements forming carbide, i.e. chromium and molybdenum, as it did in the case of steel tubes X11CrMo9-1 furnaces operated in the platformer CCR [19].

Also the qualitative distribution of carbon was performed by using a low accelerating voltage of the electron beam equal to 3 kV. The carbon content measurements were performed from 10 µm x 8 µm areas (see Fig. 6a). Quantitatively the carbon content in the surface layer can be calculated from the volume percentage of carbides in the structure, on the assumption that the whole carbon is in the carbides. Under this assumption, the carbon content at the surface is about 6-7%, and decreases with distance from the surface. At a distance of about 2 mm carbon content of the steel is 0.11%. Additionally microhardness test was also performed to determine the approximate distribution of carbon in the carburized layer. Due to the size of the indentation generated during the hardness measurement, the first measurement in each series was performed at depth of 20 µm. Fig. 6b shows the hardness profile of the steel as a function of the distance from the inner surface of the pipe, obtained from average hardness values and additionally standard deviation from each series of five measurements is indicated. On the basis of the hardness profile, the carbon distribution in the carburized layer can be qualitatively determine. As can be seen from Fig. 6b, the distribution of hardness in the carburized layer resembles a typical hardness distribution for diffusion layers. Initially, the hardness rapidly decreases, however, with increasing distance from the inner surface of the pipe fall is getting smaller and deeper than 2 mm assumes a constant value corresponding to the hardness of the steel in the core.

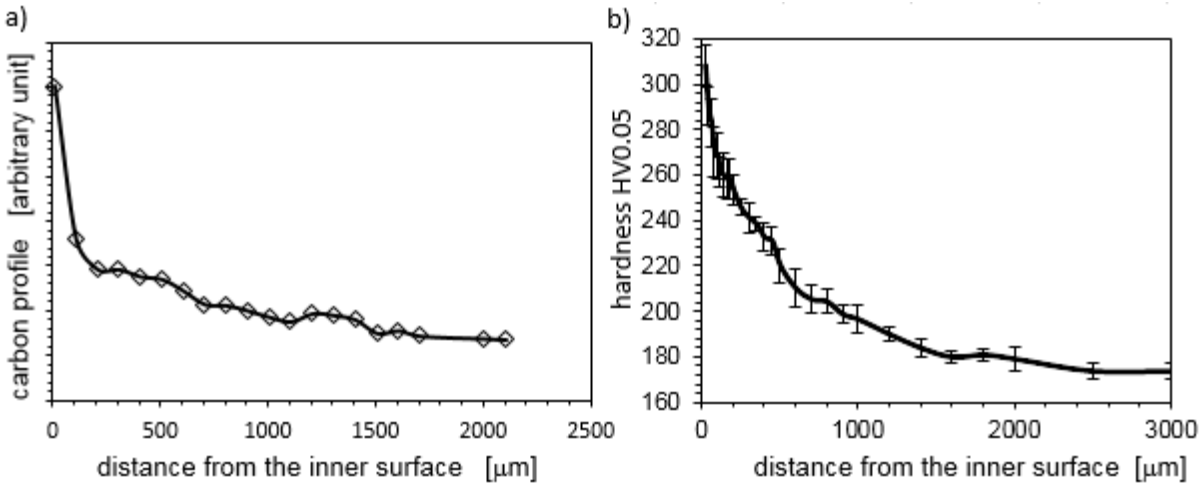

Fig. 6. Qualitative carbon distribution measured by EDS technique – Fig. a), and hardness profile of the cross-section tube after 10 years of operation in the semi-regenerative catalytic reformer – Fig. b)

In order to determine the morphology and chemical composition of the precipitates, extraction replicas were performed which then were analyzed using a TEM. The inner surface of the pipe covered with a layer of corrosion products having a thickness of about 15 µm which is shown in Fig. 7. Directly beneath the inner surface of the tube there is a layer composed of a large connected to each other precipitates which could not be extracted on a replica; only the prints of their shapes can

be observed. In the material located below this layer there are large spheroidal carbides between which are visible less precipitations of lamellar structure (Fig. 8a). Diffraction pattern of spheroidal precipitates (Fig. 8b) approximately fit both the Fe_3C and Fe_2MoC carbides. This will probably carbides $Fe_{3-x}Mo_xC$, where $x \in (0, 1)$. Diffraction pattern with a lamellar precipitates (Fig. 8c, d) approximately fit both Fe_2MoC, Fe_3C, and $M_{23}C_6$ carbides. They are likely to be undergoing transformation $M_{23}C_6 \rightarrow M_3C$ carbides. Lamellar carbides can be also observed at the bottom of large, spheroidal precipitates imprints, which could not be extracted on replica (Fig. 9). They are probably carbides, which nucleate at interfaces previously created carbide/ferritic matrix. With increasing distance from the surface of the inner tube increases the share of lamellar precipitates (Fig. 10a). Diffraction of these precipitates are equally suitable for Fe_2MoC and to Fe_3C carbides (Fig. 10b). With increasing distance from the surface of the inner tube decreases the size of spheroidal

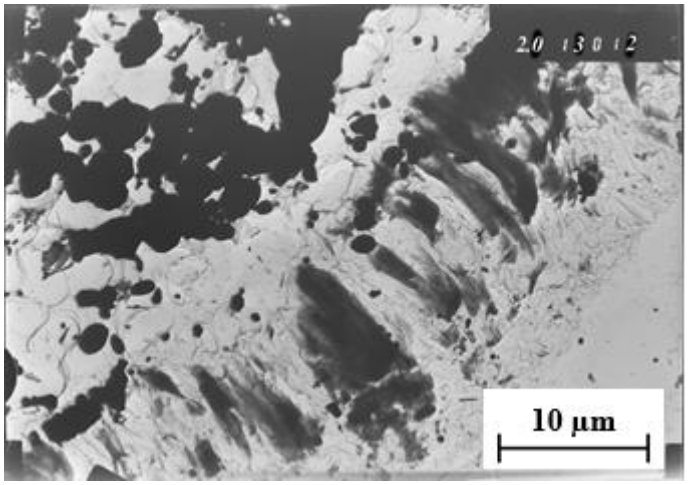

Fig. 7. The extraction replica image made on the edge of the sample. Visible parts of corrosion products on the construction of the fiber, growing perpendicular to the inner surface of the pipe, and large, spheroidal precipitation occurring in the inner surface of steel pipe, bright field

precipitates (Fig. 10c). At a depth of about 350 µm the lamellar precipitates start predominate (Fig. 11a). Diffraction pattern of these precipitates were identified as $M_{23}C_6$ type carbides. At a depth of about 500 µm there is visible a distinct predominance of lamellar precipitates (Fig. 11b). The morphology of the precipitates present in the steel at a depth greater than the thickness of the carburized layer (the core pipe) is shown in Fig. 11c. Diffraction analysis showed that the dominant type of precipitates in the core tubes are $M_{23}C_6$ type carbides (Fig. 11d).

With the help of the EDS technique, an analysis of the chemical composition of precipitates were also performed. Analysis of a layer of corrosion products determined as the distance - zero. Changes in the chemical composition of the precipitates as a function of a distance from the inner surface of the

tube are shown in Fig. 12. As is apparent from Fig. 12, the content of chromium and molybdenum in precipitates increases with increasing distance from the inner surface of the tube.

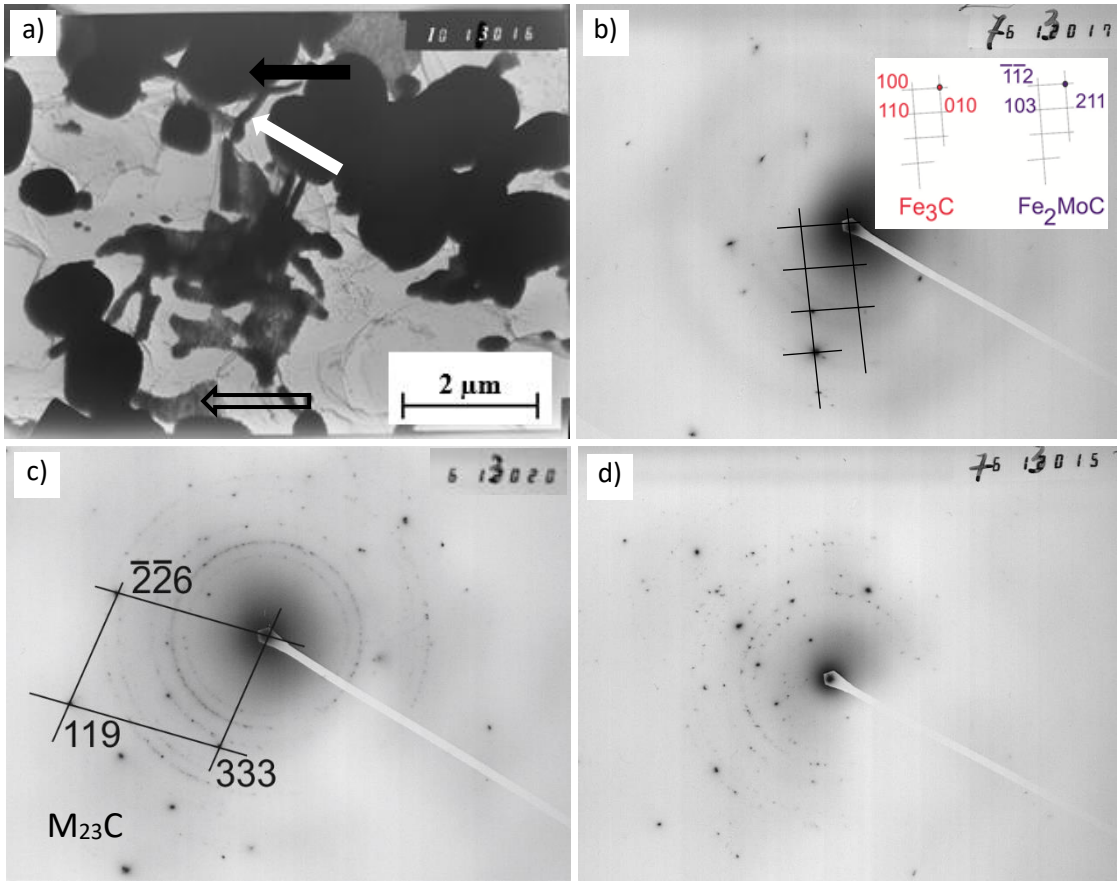

Fig. 8. Large spheroidal, and smaller lamellar precipitates occurring in the material at a distance of 5-10 µm of a continuous layer of carbide (bright field) – Fig. a). The diffraction pattern of spheroidal precipitates depicted by black arrow in Fig. a); diffraction reflections at approximately adjust both the cementite and carbide Fe_2MoC – Fig. b). The diffraction pattern of the lamellar precipitates depicted by white arrow in Fig. a) identified as $M_{23}C_6$ carbide (there are deviations of the measured Bragg angles of the table values) – Fig. c). Diffraction pattern of the lamellar precipitates depicted by the transparent arrow in Fig. a): in the best approximate fit Fe_2MoC carbide, but also cementite and carbide $M_{23}C_6$ (with a slightly larger angular misadjusts) – Fig. d)

4. Discussion

Analysis of the test results of samples of steel taken from the reformer furnace tubes after 10 years of operation showed that there are significant differences between the metal dusting mechanism developed in the laboratory, and the mechanism of destruction of 10CrMo9-10 steel exploited in

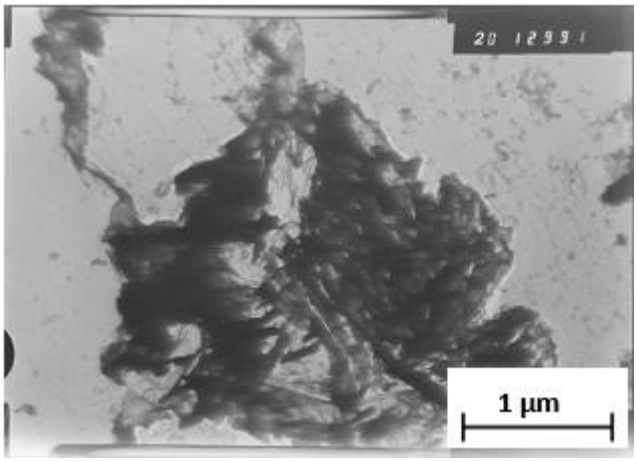

Fig. 9. Small, lamellar precipitations at the bottom of imprints, not extracted spheroidal carbide

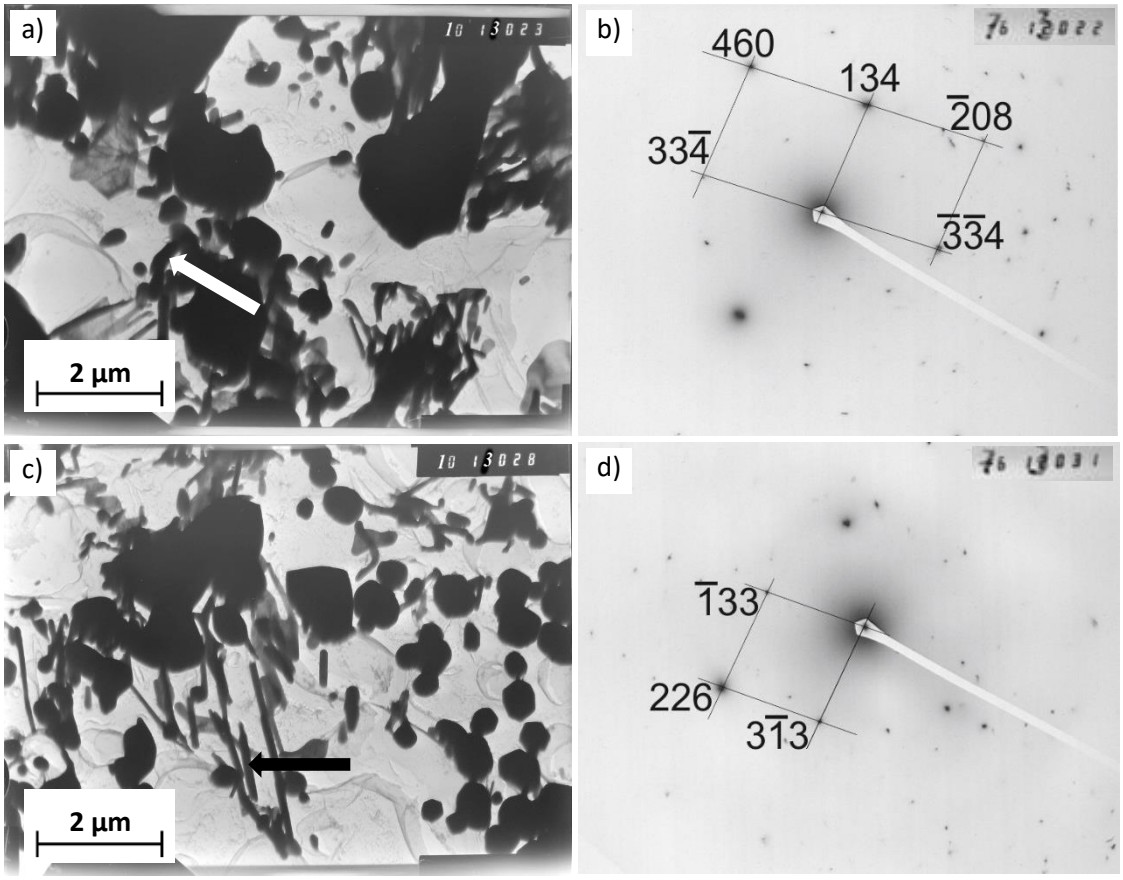

Fig. 10. Image precipitates occurring at a depth of about 50 µm (bright field) – Fig. a). The diffraction pattern of lamellar precipitates depicted by arrow and shown in Fig. a); reflections at approximately adjust both Fe_2MoC carbide as cementite, however, for both angular deviations – Fig. b). Image precipitates occurring at a depth of about 130 µm (bright field) – Fig. c). The diffraction pattern of lamellar precipitates depicted by arrow and shown in Fig. c), identified as carbide $M_{23}C_6$ – Fig. d)

industrial conditions. Elements, which are not included in the previously proposed models of corrosion, are processes of formation of M_XC_Y alloy carbides with an increase of carbon activity in the

steel (laboratory models assume that in low-alloy and unalloyed steels, metastable M_3C carbide are only formed), way of their nucleation and growth, taking into account the presence of primary carbides, and their changes as a result of long-term operation at high temperature. An important component of the corrosion mechanism from the viewpoint of operation of the equipment is to create a carburized layer with a large thickness, the presence of which could adversely affect the plastic properties of the material, which was also not observed under laboratory conditions. Carbon transport from the environment into the steel results in the increase of its activity in the surface layer of the material and form as a first stable alloy carbides $M_{23}C_6$ type, which nucleate at interfaces of primary carbides and metal matrix. Their growth results in a formation of a large spheroidal precipitates, the larger the higher activity is of the carbon in the steel, i.e. the closer the material is positioned with respect to the inner tube surface. Increasing the volume of precipitates is accompanied by the decrease the content of alloying elements in the matrix, a result of which content of these elements in emerging carbides is getting lower. The increased activity of the carbon

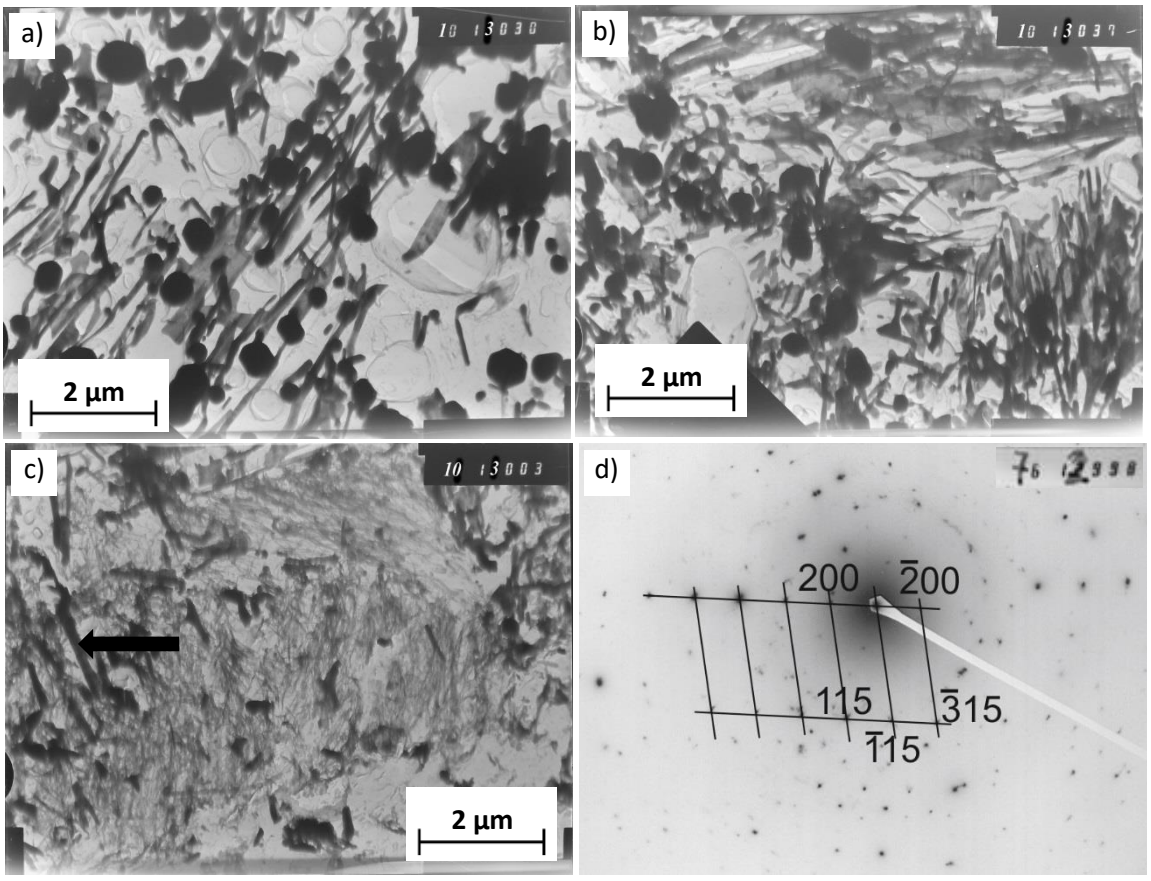

Fig. 11. Image precipitates occurring at a depth of about 350 µm – Fig. a), about 500 µm – Fig. b), and the image extraction replica at a depth greater than the thickness of the carburized layer – Fig. c) (all bright field). The diffraction pattern of lamellar precipitates depicted by arrow and shown in Fig. c), identified as $M_{23}C_6$ carbides – Fig. d)

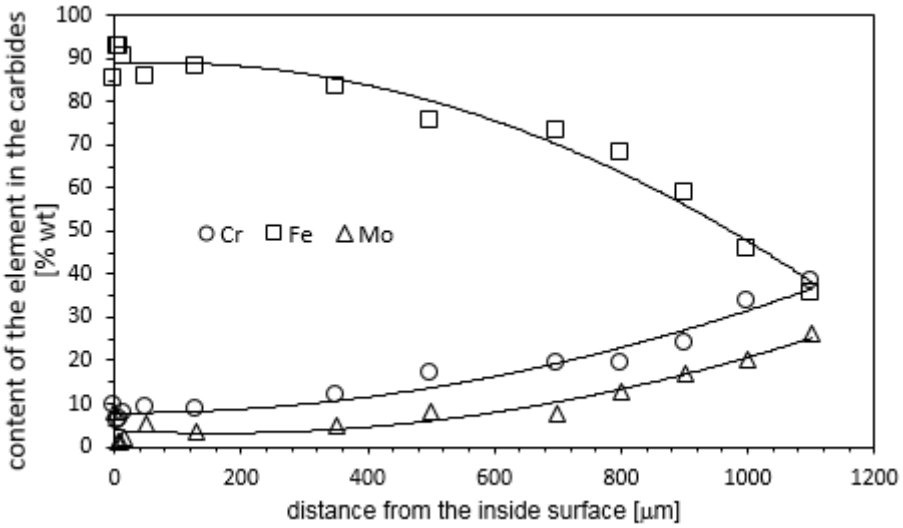

Fig. 12. Content of the chromium, molybdenum and iron in the carbides as a function of distance from the inside surface (IS) of the tube

above the equilibrium M_3C type carbide formation results in creation of these carbides. As a result of the diffusion of alloying elements within precipitates composed of a variety of carbides, and their changes resulting from long-term use of steel at high temperature, are formed low-alloy precipitates composed mainly of metastable carbides M_3C type.

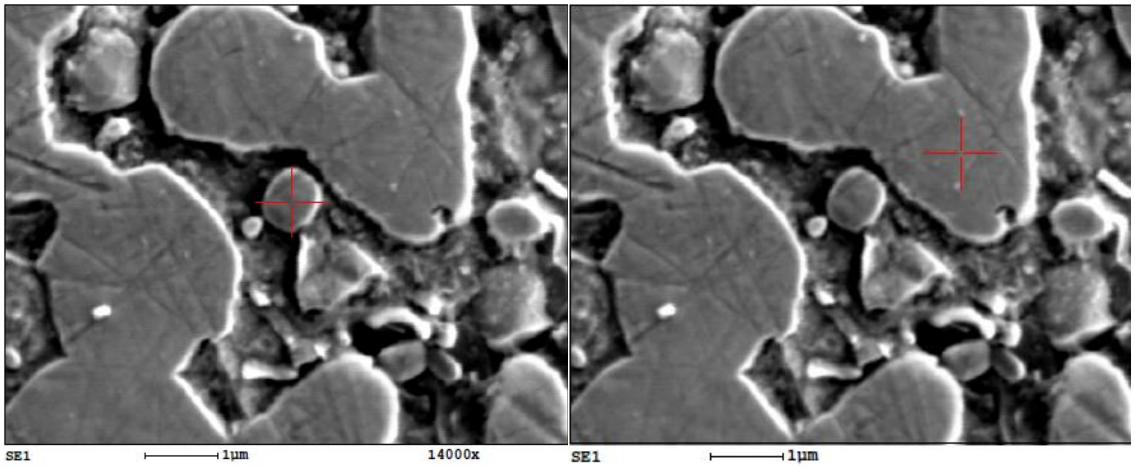

Fig. 12. …

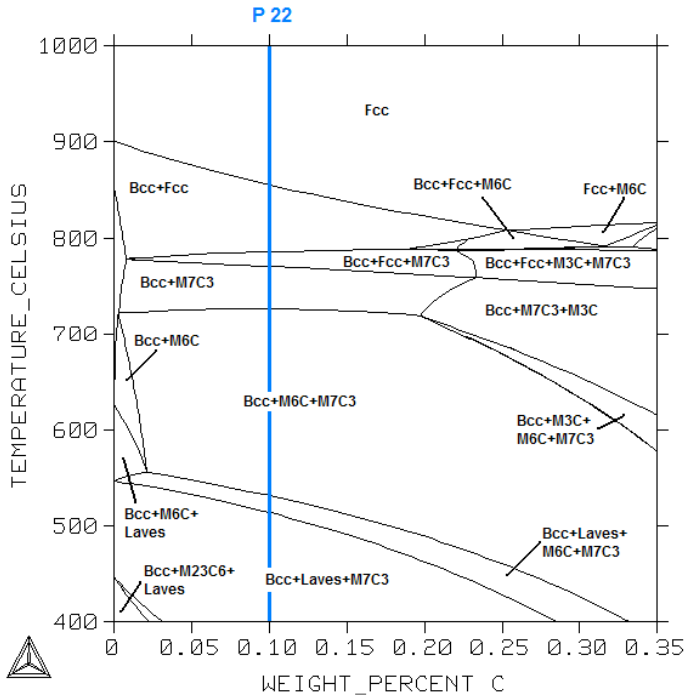

On the basis of the examinations carried out, model of metal dusting corrosion of 10CrMo9-10 steel (P22 according to ASTM) operated in an reducing environment, consisting of hydrocarbons and hydrogen was proposed.

1. 10CrMo9-10 steel in the initial state i.e. after normalizing and high tempering, has a microstructure composed of ferrite α and alloy carbide M_XC_Y (M_2C, M_6C, M_7C_3). As a result of thermal decomposition of hydrocarbons in the gaseous phase, the free carbon atoms create, which leads to increased carbon activity a_C at this phase. Free carbon atoms are adsorbed on the surface of the metallic phase, then they are absorbed and diffuse into the steel. The carbon activity in the surface layer of steel increases and ferrite alloy supersaturated by carbon α (C) is formed, as schematically shown in Fig. 9.

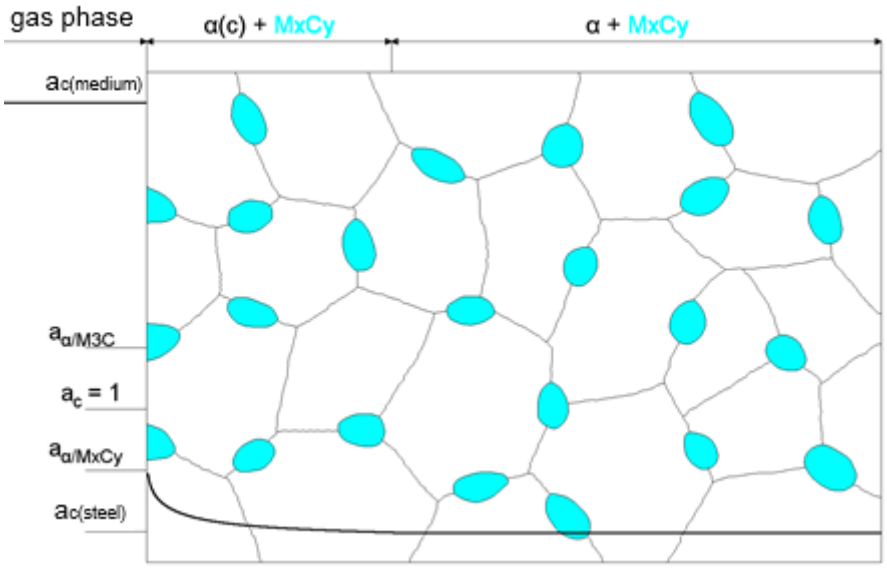

Fig. 9. Stage I - increase the carbon activity in the surface layer and the creation of ferrite alloy supersaturated by carbon (color: online only)

2. The increase in carbon activity greater than the activity of the equilibrium of M_XC_Y carbide formation ($a_{\alpha(C)}$ / MxCy) causes that at α/primary carbides MxCy interfaces, new carbides MxCy' evolve and grow, which leads to an increase in the particle size of carbide. The content of alloying elements - chromium and molybdenum in the ferrite decreases, resulting in their presence in the newly established carbides is dropping, and type of formed precipitates changes (see Fig. 10).

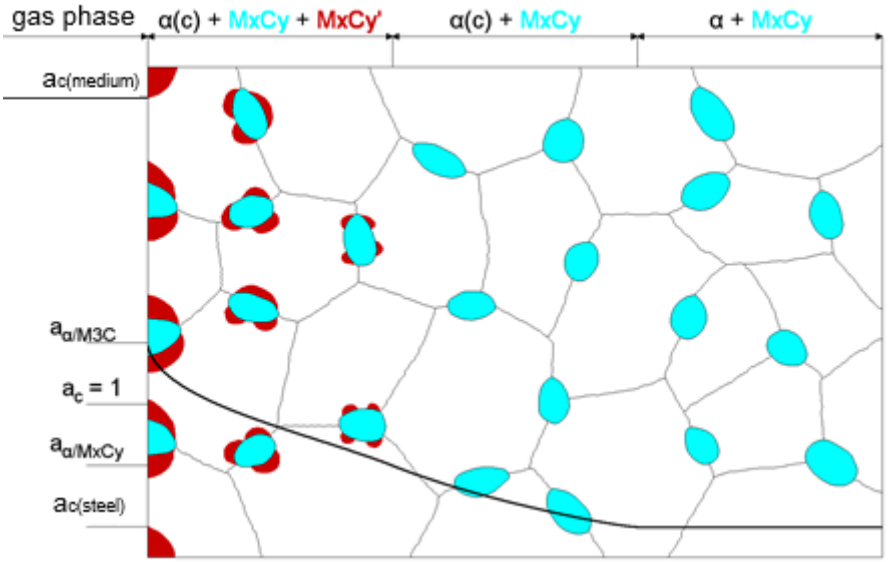

Fig. 10. Stage II - nucleation and growth of new carbide MxCy' at ferrite/primary carbides MxCy interfaces (color: online only)

3. The process of carbides precipitation decreases the carbon activity, however, continuous, intensive transport of carbon to the steel causes a further increase in carbon activity in the surface layer. The carbon precipitation process also causes continuous reduction of the content of chromium and molybdenum in the ferrite. After a decrease in the content of alloying elements in the ferrite, and after exceeding carbon activity corresponding formation of M_3C carbides ($a_C > a_{\alpha (C) / M3C}$), process of nucleation and growth of low-alloy, metastable M_3C carbides progresses at ferrite/carbide interfaces (Fig. 11).
4. Lowering the content of alloying elements in the ferrite and the processes of formation subsequent carbides on the primary carbides, coagulation, spheroidization and diffusion of elements within the carbide phases cause the formation of large spheroidal particles with a complex structure, containing the less alloying elements, the closer the metal surface they are located. Directly below the surface, where the carbon activity is the highest, the process of nucleation and growth of carbides occurs most intensely. This results in a formation of thin zone consisting solely of connected to each other carbide precipitates of a complex structure ($M_{23}C_6$, M_7C_3, M_3C), and the average chemical composition similar to that of the nominal steel. The predominant type of carbide in these precipitations is low-alloyed, metastable carbide M_3C type (Fig. 12).

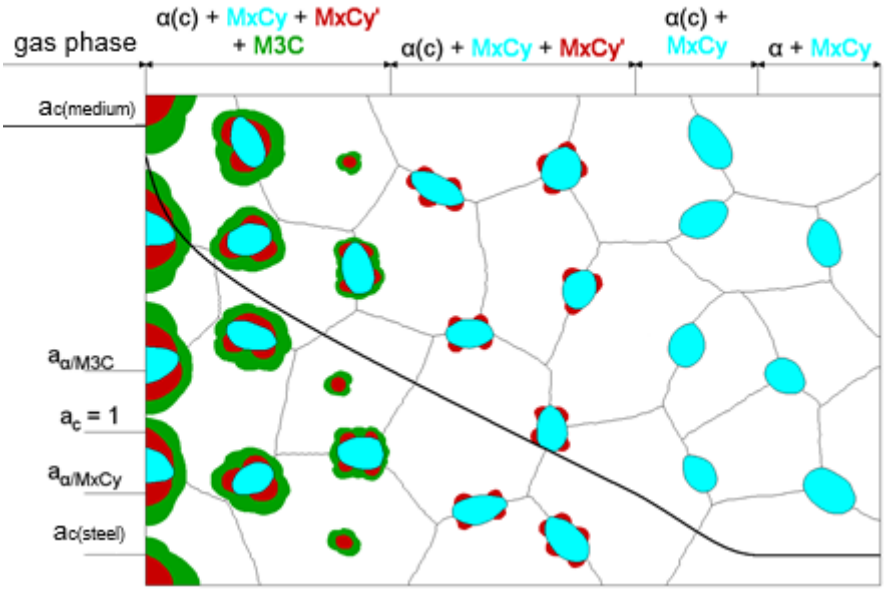

Fig. 11. Stage III - nucleation and growth of M_3C carbides at ferrite/carbides interfaces (color: online only)

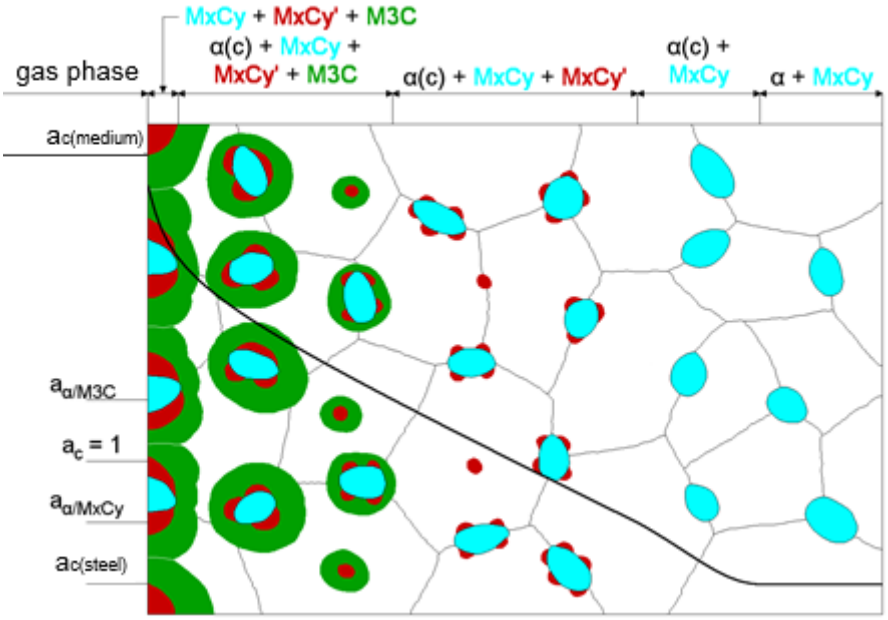

Fig. 12. Stage IV - producing a thin layer consisting of connected to each other carbide precipitates (color: online only)

5. In a steel operating in temperature of about 600 °C, transport of carbon from a vapor phase to steel is restricted due to the limited diffusion of carbon in the carbide phase [20-23]. Carbon is deposited on the surface of steel in the form of graphite, and its activity at the graphite/carbides interface is reduced to $a_C = 1$ (Fig. 13).

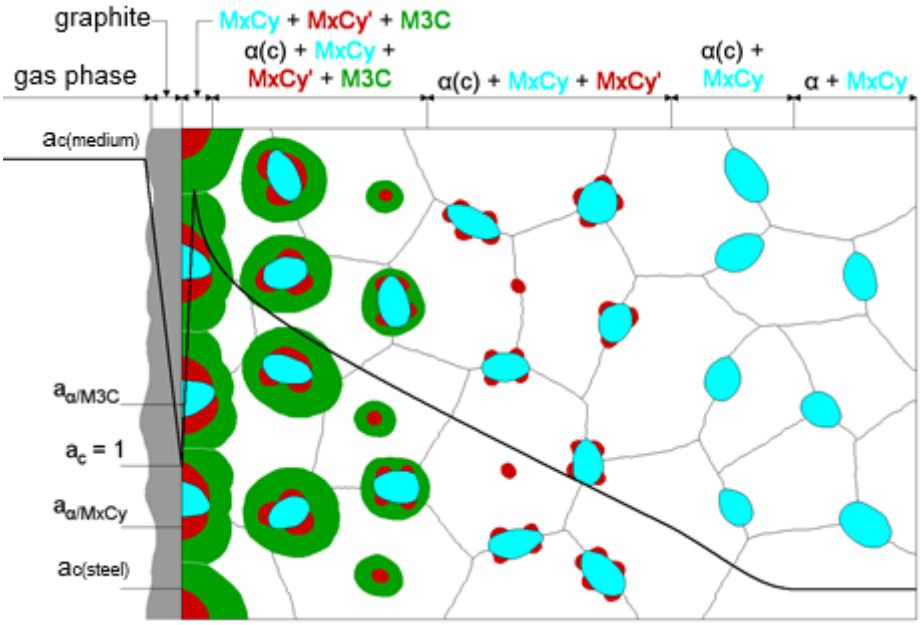

Fig. 13. Stage V - nucleation and growth of the graphite layer on the steel surface; lowering the carbon activity of the material located under a layer of graphite (color: online only)

6. Present in surface layer, low-alloyed metastable M_3C carbide, where M is mainly Fe (meaning that it is approximately cementite) becomes unstable and it starts to disintegrate in accordance with the reaction: $Fe_3C \rightarrow 3Fe + C$. The released carbon atoms attach to graphite layer ingrowing into cementite and iron atoms diffuse through the graphite layer on the outside, in accordance with the decreasing concentration gradient, where they combine into molecules capable of catalyzing further deposition of carbon from the gas phase in the form of fibers (Fig. 14).

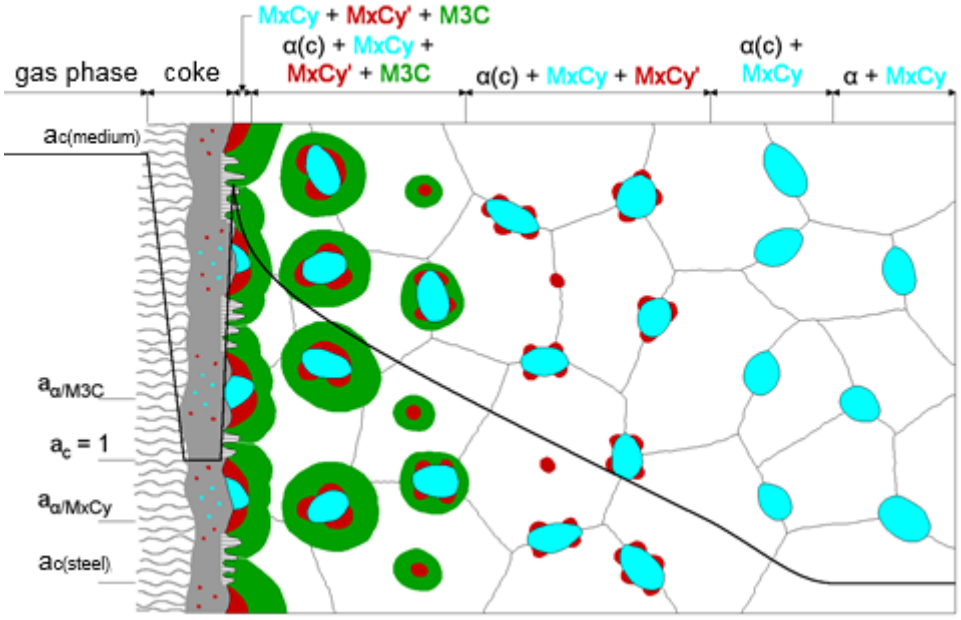

Fig. 14. Stage VI - destabilization and disintegration of low-alloy, metastable M_3C type carbides (color: online only)

5. Conclusion

The results allow the following conclusions:

1. The mechanism of metal dusting of 10CrMo9-10 steel operating at semi-regenerative catalytic reforming unit differs from the models developed on the basis of laboratory tests.
2. As a result of an increase in carbon activity in the steel, $M_xC_{y'}$ alloyed carbides precipitate in the first place what theoretical models do not take into account, however, at a later stage these carbides may convert to the metastable M_3C carbides due to prolonged operation of the steel at high temperature, low chromium content in the steel and a further increase carbon activity in the steel.
3. $M_xC_{y'}$ carbides precipitation process does not significantly affect the corrosion mechanism. While the a significant difference relative to the metal dusting mechanism models developed on the basis of laboratory tests is to create a highly carburized layer of substantially greater thickness. It is very important for the operation of the equipment. Strong carburization of steel on large depth will result in a significant deterioration in its plastic properties and as a result can contribute to a major accident due to brittle fracture of these elements.

4. The results also show that models of metal dusting mechanism can be developed on the basis of materials taken from the damaged post-operated components. In addition, this approach allows obtainment a more complete information regarding the mechanism of destruction of the elements operating in industrial installations, compared to expensive experiments conducted in laboratory conditions, which often do not reflect the operating parameters of the system.

6. References

[1] H. Ackermann, P. Karduck, H. Koehne, K. Lucka, L. Lucks, A. von Richthofen, Metal dusting in low-NOx recirculation burners for fuel oil, Corrosion Engineering, Science and Technology 40(3) (2005) 233-238.

[2] J. Z. Albertsen, Ø. Grong, R. H. Mathiesen, B. Schmid, Metallurgical investigation of metal dusting corrosion in plant-exposed nickel-based alloy 602CA, Corrosion Engineering, Science and Technology 40(3) (2005) 239-243.

[3] M. J. Bennett, Carbon deposition: A major technological problem, Materials and Corrosion 49 (1998) 345-351.

[4] F. Dettenwanger, D. Grotmann, H. Friedrich, E. Berghof-Hasselbächer, M. Schorr, M. Schűtze, Damage of a heat-treatment retort by metal dusting attack. Materials and Corrosion 50 (1999) 289-293.

[5] H. J. Grabke, Corrosion of alloy 600 in a carburization furnace, Materials and Corrosion 52 (2001) 546-551.

[6] R. H. Krikke, J. Hoving, K. Smit, Monitoring the carburization of furnace tubes in ethylene plants, Materials Performance (1976) 9-14.

[7] D. Lopez-Lopez, A. Wong-Moreno, A. Teran-Sarabia, A. Velasco-Tellez, L. Martinez, Mechanistic aspects of carburization in oil-fired power plants, Materials and Corrosion 49 (1998) 272-277.

[8] H. J. Grabke, Metal dusting of low- and high-alloy steels, Corrosion 51 (9) (1995) 711-720.

[9] R. F. Hochman, Catastrophic deterioration of high temperature alloys in carbonaceous atmospheres, Proceedings of the Symposium on properties of High Temperature Alloys 1976 715-732.

[10] L. D. Burns, Corrosion on new distillation unit processing low sulfur crude, Corrosion 6 (1950) 169-177.

[11] H. J. Grabke, M. Schütze, Corrosion by carbon and nitrogen, European Federation of Corrosion Publications No 41. 162.

[12] F. Eberle, R. D. Wylie, Attack on metals by synthesis gas from methane-oxygen combustion, Corrosion 15 (1959) 622t-626t.

[13] C. M. Chun, T. A. Ramanarayanan, J. D. Mumford, Relationship between coking and metal dusting, Materials and Corrosion 50 (1999) 634-639.

[14] H. J. Grabke, C. B. Bracho-Troconis, E. M. Műller-Lorenz, Metal dusting of low alloy steels, Werkstoffe und Korrosion 45 (1994) 215-221.

[15] H. J. Grabke, R. Krajak, E. M. Müller-Lorenz, Metal dusting of high temperature alloys, Materials and Corrosion 49 (1998) 89-97.

[16] H. J. Grabke, R. Krajak, J. C. Nava Paz, On the machanism of catastrophic carburization: Metal dusting, Corrosion Science 35 (1993) 1141-1150.

[17] H. J. Grabke, Metal dusting, Materials and Corrosion 54(10) 2003 736-746

[18] H. J. Grabke, Thermodynamics, mechanisms and kinetics of metal dusting, Materials and Corrosion 49 (1998) 303-308.

[19] J. Dampc, Z. Grzesik, J. Hucińska, Metal dusting in CCR platforming unit, Materials and Corrosion, 60 (2009) 211-217.

[20] Zs. Tokei, H. Viefhaus, H. J. Grabke, Initial stages of oxidation of a 9CrMoV steel: role of segregation and martensite lath, Applied Surface Sci. 165 (2000) 23-33.

[21] E. T. Turkdogan, J. V. Vinters, Catalytic effect of iron on decomposition of carbon monoxide. I. Carbon deposition in H_2-CO mixtures, Metallurgical and Materials Transactions B-Process Metallurgy and Materials Processing Science 5 (1974) 11-19.

[22] K. T. Voisey , Z. Liu, F. H. Stott, Inhibition of metal dusting of Alloy 800H by laser surface melting, Applied Surface Science 252(10) (2006) 3658-3666.

[23] P. L. Walker , J. F. Jr. Rakszawski , G. R. Imperial, Carbon mixture over iron catalysts. II. Rates of carbon formation, Journal of Physical Chemistry 63(2) (1959) 140-149.

[24] Z. Zeng, K. Natesan, V. A. Maroni, Investigation of metal-dusting mechanism in Fe-base alloys using Raman spectroscopy, X-Ray diffraction, and electron microscopy, Oxidation of Metals 58 (2002) 147.

[25] M. A. A. Motin, J. Zhang , P. R. Munroe, D. J. Young, Internal oxidation and metal dusting of Fe–Si alloys, Corrosion Science 52 (2010) 3280–3286.

[26] C. M. Chun, T. A. Ramanarayanan, Metal-dusting corrosion of low-chromium steels, Oxidation of Metals 62 (2004) 71-92.

[27] A. R.-V. Put, K. A. Unocic, M. P. Brady, B. A. Pint, Performance of chromia- and alumina-forming Fe- and Ni-base alloys exposed to metal dusting environments: The effect of water vapor and temperature, Corrosion Science 92 (2015) 58–68.

[28] J. Zhang, D. J. Young, Contributions of carbon permeation and graphite nucleation to the austenite dusting reaction: A study of model Fe–Ni–Cu alloys, Corrosion Science 56 (2012) 184–193.

[29] M. Li, Y. Zhu, C. Zhou, Effect of yttrium on the coking behavior of Fe-based superalloy in heavy hydrocarbon, Corrosion Science, In Press, Accepted Manuscript, Available online 30 May 2015

[30] A. Fabas, D. Monceau, S. Doublet, A. R.-V. Put, Modelling of the kinetics of pitting corrosion by metal dusting, Corrosion Science, In Press, Accepted Manuscript, Available online 6 June 2015

Figure Captions

Fig. 1. Schematic diagram of a typical semi-regenerative catalytic unit in a petroleum refinery 1 – fired heater, 2 – fixed bed reactor, 3 – pump, 4 – compressor, 5 – gas separator, 6 – cooler, 7 – pressure controller, 8 – feed (hydrotreated naphtha and recycle hydrogen gas), 9 – preheater, 10 – net hydrogen

Fig. 2. View of cut portion of the tube furnace No 12

Fig. 3. The cross section of P22 steel pipe after 10 years of operation in the semi-regenerative catalytic reformer

Fig. 4. Images obtained with the cross section of the tube. The inner surface of the pipe with the subsurface layer – Fig. a). Microstructure of the steel approximately 150 μm from the inner surface of the pipe – Fig. b), 500 μm from the surface – Fig. c), 750 μm from the surface – Fig. d), 1 mm from the surface – Fig. e), 3 mm from the surface – Fig. f)

Fig. 5. Average content of the chromium and molybdenum in the steel as a function of distance from the inside surface (IS) of the tube

Fig. 6. Qualitative carbon distribution measured by EDS technique – Fig. a), and hardness profile of the cross-section tube after 10 years of operation in the semi-regenerative catalytic reformer – Fig. b)

Fig. 7. The extraction replica image made on the edge of the sample. Visible parts of corrosion products on the construction of the fiber, growing perpendicular to the inner surface of the pipe, and large, spheroidal precipitation occurring in the inner surface of steel pipe, bright field

Fig. 8. Large spheroidal, and smaller lamellar precipitates occurring in the material at a distance of 5-10 μm of a continuous layer of carbide (bright field) – Fig. a). The diffraction pattern of spheroidal precipitates depicted by black arrow in Fig. a); diffraction reflections at approximately adjust both the cementite and carbide Fe_2MoC – Fig. b). The diffraction pattern of the lamellar precipitates depicted by white arrow in Fig. a): identified as $M_{23}C_6$ carbide (there are deviations of the measured Bragg angles of the table values) – Fig. c). Diffraction pattern in the best approximate fit Fe_2MoC carbide, but also cementite and carbide $M_{23}C_6$ (with a slightly larger angular misadjusts) – Fig. d)

Fig. 9. Image precipitates occurring at a depth of about 50 μm (bright field) – Fig. a). The diffraction pattern of lamellar precipitates depicted by arrow and shown in Fig. a); reflections at approximately adjust both Fe_2MoC carbide as cementite, however, for both angular deviations – Fig. b). Image precipitates occurring at a depth of about 130 μm (bright field) – Fig. c). The diffraction pattern of lamellar precipitates depicted by arrow and shown in Fig. c), identified as carbide $M_{23}C_6$ – Fig. d)

Fig. 10. Image precipitates occurring at a depth of about 350 µm – Fig. a), about 500 µm – Fig. b), and the image extraction replica at a depth greater than the thickness of the carburized layer – Fig. c) (all bright field). The diffraction pattern of lamellar precipitates depicted by arrow and shown in Fig. c), identified as $M_{23}C_6$ carbides – Fig. d)

Fig. 11. Content of the chromium, molybdenum and iron in the carbides as a function of distance from the inside surface (IS) of the tube

Fig. 12. ……

Fig. 13. Stage I - increase the carbon activity in the surface layer and the creation of ferrite alloy supersaturated by carbon

Fig. 14. Stage II - nucleation and growth of new carbide MxCy' at ferrite/primary carbides MxCy interfaces

Fig. 15. Stage III - nucleation and growth of M3C carbides at ferrite/carbides interfaces

Fig. 16. Stage IV - producing a thin layer consisting of connected to each other carbide precipitates

Fig. 17. Stage V - nucleation and growth of the graphite layer on the steel surface; lowering the carbon activity of the material located under a layer of graphite

Fig. 18. Stage VI - destabilization and disintegration of low-alloy, metastable M3C type carbides

Tables

Table 1. Characteristics of steel tested and the service conditions

Table. 2. The content of elements at different distances from the inner surface of the tube measured by EDS